The interdependence of structural and electrical properties in TiO2/TiO/Ti periodic multilayers

Arnaud Cacucci, Ioannis Tsiaoussis, Valérie Potin, Luc Imhoff, Nicolas Martin, Tomas Nyberg

The interdependence of structural and electrical properties in TiO_2/TiO/Ti periodic multilayers

Arnaud CACUCCI [(a)], Ioannis TSIAOUSSIS [(a)], Valérie POTIN [(a)], Luc IMHOFF [(a)], Nicolas MARTIN [(b, c) *], Tomas NYBERG [(c)]

[(a)] ICB - Laboratoire Interdisciplinaire Carnot de Bourgogne, UMR 6303 CNRS - Université de Bourgogne
9, Avenue Alain Savary, BP47870, 21078 DIJON Cedex, France

[(b)] Institut FEMTO-ST, UMR 6174, Université de Franche-Comté, CNRS, ENSMM, UTBM
32, Avenue de l'observatoire, 25044 BESANCON Cedex, France

[(c)] Solid State Electronics, The Ångström Laboratory, Uppsala University
Box 534, 75121 UPPSALA, Sweden

Abstract

Multilayered structures with 14 to 50 nm periods composed of titanium and two different titanium oxides, TiO and TiO_2, were accurately produced by DC magnetron sputtering using the reactive gas pulsing process (RGPP). Structure and composition of these periodic TiO_2/TiO/Ti stacks were investigated by X-ray diffraction (XRD) and transmission electronic microscope (TEM) techniques. Two crystalline phases hcp-Ti and fcc-TiO were identified in the metallic-rich sub-layers whereas the oxygen-rich ones were made of a mixture of amorphous TiO_2 and rutile phase. DC electrical resistivity ρ measured for temperatures ranking from 300 to 500 K exhibited a metallic-like behaviour (ρ_{473K} = 1.05×10^{-5} to 1.45×10^{-6} Ω m) with a temperature coefficient of resistance (TCR) ranging from 1.20×10^{-3} K^{-1} for the highest period Λ = 50.0 nm down to

negative values close to -4.97×10^{-4} K^{-1} for the smallest one Λ = 14.0 nm. A relationship between the dimensions of periodic layers and their collective electrical resistivity is proposed where the resistivity does not solely depend on the total thickness of the film, but also on the chemical composition and thickness of each sub-layer. Charge carrier mobility and concentration measured by Hall effect were both influenced by the dimension of TiO_2/TiO/Ti periods and the density of ionized scattering centres connected to the titanium concentration in the metallic sub-layers.

Keywords

Multilayers, titanium oxides, HRTEM, periodic structure, electrical properties

* Corresponding author, Tel.: +33 (0)3 81 85 39 69, Fax: +33 (0)3 81 85 39 98, Email: nicolas.martin@femto-st.fr

Highlights

- TiO_2/TiO/Ti periodic multilayers are deposited by reactive sputtering.
- Nanometric periods from 14 to 50 nm are precisely produced by gas pulsing.
- Hcp-Ti and fcc-TiO phases are found in the metallic sub-layers whereas amorphous and rutile compounds are detected in the TiO_2 sub-layers.
- TCR of films exhibiting metallic-like behaviour can be tuned from positive to negative.
- Carrier mobility and concentration are connected to the density of ionized scattering centres.

1. Introduction

For many decades, metal oxide thin films, especially titanium-based coatings, have attracted much attention in various fields because of their remarkable physical, chemical and biological properties. They are largely involved in a wide range of applications such as antireflective coatings, gas sensors, biomedical devices, photocatalysts, etc [1-8]. In addition to the intrinsic properties of titanium oxide films (metal, semiconductor, insulator according to the oxygen content), some of their behaviours can also be tailored playing on the nanostructure. It becomes of particular interest when the structuration is performed throughout the whole thickness of the film which may be accomplished in periodic metal/oxide multilayers. The resulting properties (especially the electronic conductivity) can be strongly influenced by the dimensions and the quality of the metal/oxide periods and interfaces. Consequently, structural and interfacial characteristics have to be taken into account to understand the electronic transport properties.

First of all, the fabrication of regular and periodic alternations appears as a relevant challenge, especially with periodic multilayers involving titanium because of its strong reactivity towards oxygen. Many deposition methods have been developed to prepare titanium oxide films [9-15]. However, few deposition processes allow the preparation of metal/oxides nanometric multilayers with abrupt and well-controlled interfaces [16-18]. Among these methods, the reactive sputtering may be an attractive approach to prepare periodic structures at the nanometric scale. However, the reactive sputtering technique normally exhibits hysteresis effects, which makes it difficult to operate the process to obtain certain film compositions [19-22]. Some well-tested approaches like high pumping speeds, feedback control systems or more specific devices were developed to overcome the problems associated with such instabilities [23-26]. Such improvements

have made it possible to prepare metal oxide thin films with tuneable chemical compositions.

In a previous work [27], the combination of DC magnetron sputtering and the reactive gas pulsing process (RGPP) resulted in an accurate and reproducible structuration of titanium oxide multilayers at the nanometric scale. Although these performances, the idea is also to turn a sensitive material into a directly applicative and simple device for gas sensors by melding electrical properties of a metal and an insulator sub-layers. Many methods of gas detection can be found [28], but the simplest and the most frequently used in the field of sensors is an electrical characterization by performing a resistivity measurement [29]. The resistivity of a material depends among others, on the temperature (this dependence is specific to the material) and is characterized by a temperature coefficient of resistivity for metals. In order to obtain a temperature invariant resistivity, the addition of dopant in the material is sometime required but sometime leads to significant manufacture over costs. Thus, the changes of resistivity could only be due to the electrical contribution of some gaseous species adsorbed at the air/film interface. In TiO_2/TiO/Ti thin periodic multilayers, only the TiO_2 compound has been employed as gas sensor [30]. This compound exhibits semiconducting-like behaviours [31] since its resistivity exponentially decreases as a function of the temperature. On the other hand, hcp-Ti and fcc-TiO are metallic phases and their electrical resistivity linearly increases versus the temperature (positive temperature coefficient of resistance).

In this article, the structural parameters of multilayered periodic TiO_2/TiO/Ti thin films including the internal nanostructure evolution are investigated. These periodic stacks are sputter deposited by reactive sputtering using the reactive gas pulsing process (RGPP) [32]. Period of the multilayers is systematically changed from 14.0 to 50.0 nm. A study

of the resistivity versus temperature is performed in order to understand the relationship between the electronic transport properties and the structural characteristics of the films. The thickness of each sub-layer associated to the well-controlled nanometric structuration produce electrical characteristics, which give rise to a metallic-like behaviour with positive and negative temperature coefficients of resistance. A theoretical relationship between resistivity, dimension of the TiO_2/TiO/Ti periods and chemical composition is finally proposed. Charge carrier concentrations and mobilities are also investigated so as to better understand their contribution in the electrical conduction characteristics.

2. Experimental details

Multilayers were simultaneously deposited onto (100) Si and glass substrates by DC reactive magnetron sputtering from a titanium metallic target (purity 99.6 at. % and 51 mm diameter) in an Ar + O_2 gas mixture. The target was sputtered with a constant current density $J = 100$ A m^{-2}. The distance between the target and the unheated substrate was fixed at 65 mm. The gas flow rates were controlled by a homemade system. All depositions were carried out with an argon flow rate of 2 sccm and a constant pumping speed of 13.5 L s^{-1}, which produced an argon partial pressure of 0.25 Pa. Oxygen mass flow rate was periodically controlled versus time according to a rectangular signal versus time by the reactive gas pulsing process, namely RGPP [32]. The pulsing period T_P of the oxygen flow rate was varying from 313 to 1000 s. During each period, the flow rate was periodically modulated with a t_{on} injection time which is a fraction of the total period T_P. The maximum O_2 flow rate was fixed at 4 sccm during the t_{on} injection time. This oxygen flow corresponds to a processing point in compound mode if the flow would be kept constant. Otherwise it was completely stopped (no oxygen injection)

during the t_{off} time. The multilayer period thickness Λ is expected to be in-between 15 to 50 nm, with $\Lambda = \lambda_{met} + \lambda_{ox}$, where λ_{met} and λ_{ox} correspond to the thickness of the metal and oxide sub-layers, respectively. As a result, the duty cycle α defined as the ratio t_{on}/T_P takes values from 72 to 90 % in order to tune the $\lambda_{met}/\lambda_{ox}$ ratio. Moreover, the deposition procedure always started with the O-rich sub-layer and finished with the Ti-rich one, the total film thickness t_{tot} being close to 400 nm.

The crystalline structure was analyzed by X-ray diffraction (XRD) in $\theta/2\theta$ configuration using a monochromatized Co Kα radiation. Scans were performed with a step of 0.02° per 0.2 s and a 2θ angle ranging from 20 to 80°. Then, for all samples the local structure was characterized by high resolution transmission electron microscopy (HRTEM). The elemental chemical composition was determined by energy-dispersive X-ray spectroscopy (EDX) with a TEM JEOL 2100 FEG operating at 200 kV (scanning probe of 2 nm). The scanning technique of TEM (STEM) was used to get local and precise chemical analyses at the nanometric scale, to discriminate each sub-layer, and to determine their thickness. Moreover, dark field imaging was applied to provide a greater contrast between the different phases.

DC electrical resistivity ρ of the films deposited on glass substrates was performed versus temperature from 300 to 500 K with a homemade system based on the van der Pauw method. In order to warrant the Ohmic behavior of the four contacts, I-V curves were systematically plotted and the linear evolution was checked for all van der Pauw combinations. Two cycles of measurements were carried out on each sample. The first cycle started at room temperature and sample was heated up to 500 K with a ramp of 2 K min^{-1} followed by a plateau for 10 min at 500 K. Afterwards, the temperature was decreased with the same ramp down to 300 K and the second cycle continued with the temperature profile as the first cycle. Similarly, charge carrier mobilities and

concentrations were obtained by Hall Effect using the same procedure as resistivity measurements but applying a perpendicular magnetic field of 0.8 Tesla to the sample surface.

3. Results and discussion

3.1 Crystallographic structure by XRD

For all diffractograms (Fig. 1), two main peaks are recorded at 2θ = 33.3 and 55.5°, which are attributed to the silicon (111) and (311) planes, respectively. The presence of this two silicon intense peaks is due to the substrate contribution as the deposit thickness is lower than 450 nm. Two other significant peaks at 2θ = 40.98 and 43.25° are also detected, but they can not be related to the same crystallographic phase. For the first one, an interplanar distance equal to d = 0.255 nm is obtained, which corresponds to the (100) planes of the hexagonal phase of metallic titanium whereas for the second one, the interplanar d-spacing is 0.241 nm. This latter is due to the (111) planes of the fcc-TiO phase.

For the shortest period Λ = 14.0 nm, no diffracted signals are detected. The size of crystalline domains is certainly lower than a couple of nanometers because the growth is periodically disturbed by the pulsing introduction of the oxygen gas. The long range order increases with the period thickness Λ. An increase of the peak intensity located at 2θ = 40.98° is clearly observed as the period Λ rises from 14.0 to 40.0 nm. It is worth noticing the absence of diffracted signals corresponding to the crystalline TiO_2 phases, either anatase or rutile, which are the most common phases for such kind of oxide compounds. This could be explained by the weakness of the signal produced by small nanocrystallites of TiO_2 (rutile or anatase phase) embedded in an amorphous TiO_2 matrix. In order to go further into the microstructure, TEM analyses have been carried

171 out on different locations of the mainly amorphous TiO_2 matrix and to reveal the
172 phase(s) in these nanocrystals, as it will be presented in the next paragraph.
173
174 ***3.2 Structure by TEM***
175 TEM observations on the cross-section of the different specimens show that the
176 alternation of the sub-layers is clearly visible with a regular periodic structure (Fig. 2).
177 The total thickness t_{tot} of the films is 345 and 405 nm, respectively (Fig. 2a and 2c).
178 Similarly, the total thickness t_{tot}, metallic and oxide sub-layers λ_{met} and λ_{ox}, respectively,
179 and the period Λ have been measured for all samples as reported in table 1. The sample
180 references with different periods and the Ti metal concentration are also indicated. These
181 TEM observations show that the dimension of the period stacks (two sub-layers) is
182 accurately controlled during the growth and remains constant from the substrate-film to
183 the film-air interface. TEM micrographs systematically indicate that the interface
184 between the silicon substrate and the grown multilayers is flat and regular, the thickness
185 of the native SiO_x layer being close to 3.0 nm.
186 In bright field mode (BF in figures 2a and 2c), 23 bright and dark bands alternations are
187 visible for the sample with Λ = 14.0 nm, whereas 8 bright and dark bands for the sample
188 with Λ = 50.0 nm. These bright and dark bands correspond to the oxide and metallic sub-
189 layers, respectively whereas in DF mode, it is the opposite. In dark field mode (DF), the
190 period thickness is accurately measured (± 0.1 nm) and the difference of sub-layers
191 crystallinity is evidenced (Fig. 2b and 2d). For the sample with the lowest period Λ =
192 14.0 nm, the metallic sub-layer thickness (λ_{met}) and the oxide one (λ_{ox}) is equal to 6.0 and
193 8.0 nm, respectively. DF image from the sample with Λ = 50.0 nm observed with a low
194 magnification (× 15 000) shows an alternation of wider dark and bright bands, with the
195 metallic sub-layer λ_{met} = 35.0 nm and the oxide one λ_{ox} = 15.0 nm. From our operating

196 conditions and assuming the deposition rates of titanium and titanium oxide, the period Λ
197 of such multilayers is expected to be in-between 15.0 to 50.0 nm, which is in good
198 agreement with the TEM measurements.
199 The crystalline quality of the sub-layers has also been studied in DF mode. The presence
200 of small bright domains in DF images indicates that the structure is partially
201 nanocrystalline (Fig. 2b) and that the Ti metallic sub-layer is better crystallized than the
202 oxide one (Fig. 2d). Moreover, a columnar structure is also pointed out in figure 2d, as
203 well as the presence of numerous defects close to the crystalline part. Consequently, the
204 crystallization is not homogeneous through the multilayered structure.
205 Combining EDX and DF experiments, it is possible to go further through the interface
206 characteristics between each sub-layer. It is pointed out that the darkest areas correspond
207 to the mostly amorphous oxide sub-layers (λ_{ox}), whereas the brightest ones correspond to
208 crystallized Ti-rich ones (λ_{met}). In each sample, every oxide sub-layer is composed of a
209 TiO_2 stoichiometric phase from the bottom to the top of the deposit. The titanium
210 concentration $C_{\lambda met}$ in the metallic sub-layers is kept constant in a given sample but
211 changes from a sample to another. Then, HRTEM observations confirmed that the
212 interfaces are distinguishable, and can be very flat in the less crystalline part of the
213 deposits.
214
215 ***3.3 HRTEM analyses***
216 HRTEM observations indicate that the metal/oxide periodic structure is very regular
217 through the whole thickness. The sub-layer thicknesses do not change during the growth
218 process in each period Λ as typically shown in the HRTEM micrograph for a period Λ =
219 50.0 nm (Fig. 3a). A magnified area (Fig. 3b) allows a more detailed viewing of the
220 column going through all the oxide and metallic sub-layers. It also confirms that the

growth continues in spite of the pulsing process. Moreover, if the growth of the metallic sub-layer occurs on a column composed of crystallized TiO_2 phase (anatase or rutile), a distortion phenomenon of the metallic sub-layer in the growth direction is observed, which create defects and prevents the deposition of perfectly parallel multilayers to the silicon surface. Selected area electron diffraction patterns (SAED) pointed out a nanocrystalline structure and the presence of significant amounts of titanium-based compounds in all specimens. SAED patterns are more sensitive than XRD measurements to identify the different phases in a material at the nanometre scale. Indeed, this study shows that the occurrence of nanocrystals increases with the thickness of the period Λ. For each sample, only TiO_2 nanocrystals are present in the O-rich sub-layer λ_{ox}. The crystallite size increases as function of the sub-layer thickness from $\lambda_{ox.}$ = 5.0 to 25.0 nm. The metal sub-layer (Ti-rich) is more crystallized and exhibits two different crystal phases: hcp-Ti and fcc-TiO. Samples with small periods (Λ < 17.0 nm) are mainly composed by fcc-TiO crystals in the metal sub-layers. For intermediate periods (17.0 < Λ < 35.0 nm) as well as the largest (Λ > 35.0 nm) the hcp-Ti crystalline phase appears (for λ_{met} > 7.0 nm), which prevails over the fcc-TiO one. This highlights that although the crystallite size increases as a function of the Λ period, TiO_2 remains the only crystalline phase in the O-rich sub-layer while the hcp-Ti phase becomes predominant compared to the fcc-TiO one as the thickness of the metal sub-layer gradually increases. In order to better understand the nanostructure, each phase and sub-layer are described in more details in the next paragraphs according to some arbitrary outlines (Parts A to E) as presented in figure 3b for a period Λ = 50 nm.

3.3.1 Poorly crystallized domains – Parts A and B

HRTEM micrographs show that the oxide sub-layers are mainly amorphous (part A). The

246 entire oxide sub-layer is made of more than 75 % of this amorphous part A. The
247 proportion depends on the thickness of the period Λ. When it increases from Λ = 14.0 to
248 45.0 nm, the amorphous part reduces from 95 down to 75 % (roughly estimated by
249 HRTEM). This reduction allows the development of a crystalline columnar structure
250 (TiO_2 grains) as described later for part C. In this pseudo-crystallization, an interplanar
251 distance d = 0.350 nm have been measured, which is close to the theoretical value d_{101} =
252 0.352 nm of the anatase phase. However, this measurement has only been performed for
253 few crystallographic planes and the poor occurrence of this phase is not representative to
254 the part A.
255 After this oxide sub-layer, the metallic one grows. The latter is mostly crystallized, but
256 two zones can be defined. The first zone contains the part B and is just over the A one. It
257 presents a lower content of crystallized grains than the parts D and E, which are in the
258 second zone of the metallic sub-layer. As previously described from EDS and TEM data,
259 the stacking is homogenous through the thickness λ_{met} of the metallic sub-layer. The
260 crystallinity only differs between the two zones. In the part B, HRTEM points out
261 crystallographic planes parallel to the interface of Si (100). Thus, these planes show a
262 preferential direction of growth. There are two interplanar distances, which appear
263 according to the growth direction. At first, an interplanar distance d = 0.240 nm is
264 measured and followed by another at d = 0.255 nm, which are close of the fcc-TiO phase
265 (d_{111} = 0.241 nm) and hexagonal titanium metal (d_{100} = 0.255 nm), respectively. Defects
266 in this sub-layer prevent from accurately locating the interface between these two
267 distances. In most of cases, the size of fcc-TiO grains exhibiting (111) orientation is 4.0
268 ± 0.5 nm, except for samples with Λ = 14.0 and 45.0 nm where the thickness of the fcc-
269 TiO grains is higher. However, samples with the metallic sub-layer thickness λ_{met} > 7.0
270 nm exhibit larger titanium grains with d_{100} = 0.255 nm (hcp-Ti phase) in the part B.

271

272 *3.3.2 Crystallized domains – Parts C, D and E*

273 These crystallized parts C, D and E are identified as crystalline columnar structure. The
274 width of these columns can reach 25 nm and be extended through the entire oxide sub-
275 layer thickness λ_{ox}. The C part faces the A part previously described (corresponding to
276 the O-rich sub-layer) whereas the D and E parts face the B one (Ti-rich one). Following
277 a column through those sub-layers helps to detail the different phases ocurring during the
278 growth from the oxide to the metallic sub-layer. In the complete crystalline part C of the
279 oxide sub-layer (Fig. 4d), [00-1] zone axes are indexed as a rutile-TiO_2 phase. The
280 interplanar distance d_{200} = 0.231 nm is very close to the theoretical value of 0.230 nm.
281 The crystallized zone of columns in oxide sub-layers is always composed of a rutile
282 phase, which grows in a preferential direction.

283 After the rutile TiO_2 phase, another crystallized zone is found by HRTEM. This zone
284 includes two parts (D and E). Taking into account the growing direction, zone axes
285 [01-1] of the fcc-TiO phase have been pointed out (part D) in figure 4c. Then, HRTEM
286 picture highlights that the hcp-Ti phase prevails (part E) and grows in the hexagonal
287 conformation with [001] zone axes (Fig. 4b). Thickness of the fcc-TiO phase is always
288 about 4 nm and the remaining thickness corresponds to the hcp-Ti one (except for
289 samples with Λ = 18.0 and 45.0 nm). Interplanar distances d_{111} and d_{100} (fcc-TiO and
290 hcp-Ti phases, respectively) also exhibit a preferential direction parallel to the substrate
291 surface. Moreover, the selected area electron diffraction pattern acquired in the columnar
292 area confirms that three families of planes grow following a parallel direction to each
293 other, but perpendicular to the growth direction. They are indexed as rutile-TiO_2-d_{200},
294 fcc-TiO-d_{111} and hcp-Ti-d_{100}, respectively (SAED in Fig. 4a). As a result, we can claim
295 that the multilayered structure is composed of a-TiO_2/rutile-TiO_2, fcc-TiO and hcp-Ti

periodic alternations. The formation of a TiO sub-layer between the TiO_2 and Ti can, to some extent, be explained by the fact that it takes a certain time to sputter away the oxide layer formed at the target surface. During this time, a TiO film will be grown.

3.4 Electrical behaviours

For all samples, the DC electrical resistivity ρ was measured in the van der Pauw configuration in the temperature range T = 300 – 500 K (Fig. 5). A linear evolution of ρ versus T was systematically observed for any multilayer with resistivity changing from ρ = 5.76×10^{-7} to 1.22×10^{-5} Ωm, which are typical of metallic-like materials. It is worth noting that four samples with the shortest period Λ (χ' = 0.338 to 0.464 defined later from equation (4)) exhibit a negative slope. In addition, resistivity is quasi constant for sample with Λ = 40.5 nm (χ' = 0.523) whereas the others behave like conventional metals, i.e. an increase of the resistivity as the temperature rises. Since the final deposited sub-layer is titanium, an increase of the period thickness Λ leads to a lower resistivity, which tends to that of pure titanium film. For metallic materials, the variation of electrical resistivity ρ is commonly connected to the temperature T using:

$$\rho = \rho_0\left[1+\alpha_0\left(T-T_0\right)\right] \quad (1)$$

with ρ_0 is the resistivity measured at T_0 = 300 K and α_0 is the temperature coefficient of resistance (TCR in K^{-1}) defined from the following relationship:

$$\alpha_0 = TCR = \frac{1}{\rho_0}\left[\frac{\partial\rho}{\partial T}\right]_{T=T_0} \quad (2)$$

As shown in table 1, positive TCR values are measured for periods Λ higher than 31.0 nm (except for Λ = 34.5 nm where TCR is negative). TCR ranges from 2.17×10^{-4} to 1.20×10^{-3} K^{-1} as the period changes from Λ = 31.0 to 50.0 nm. Resistivity as well as

TCR shift to the bulk Ti values for the thickest periods (ρ_{293K} = 3.91×10^{-7} Ωm and TCR = 5.5×10^{-3} K^{-1} for bulk titanium). However, it significantly deviates from the bulk properties as commonly observed for thin films. This is mainly attributed to the scattering of electrons at the grain boundaries [33]. Thus, the decrease of conductivity can be first related to the increasing number of grain boundaries per electron mean free path. By decreasing the period thickness Λ, electron scattering is enhanced due to the highest number of interfaces and grain boundaries since the crystallite size decreases from XRD analyses (Fig. 1). It is worth noting that for the shortest periods (Λ < 16.5 nm), the films become amorphous. No crystallite size can be significantly determined but the interfaces of the periodic TiO_2/TiO/Ti alternations are still distinguishable as shown in Fig. 2a and 2b. Thus, one can assume that the scattering effect of electrons is mainly due to interfaces. The electron mean free path (about few tens nanometers in well crystallized films) reduces and is mainly limited by the thickness of the sub-layer periods λ_{ox} and λ_{met} rather than the grain boundaries. In addition, because of the substantial amount of oxygen in the metallic sub-layer, the defect concentration rises as well, which contributes to the electron scattering and thus, to the high resistivity and low TCR values. The defects can be point defects (vacancies, interstitials), grain boundary discontinuities and 2D defects (dislocations, stacking faults) generated by interfaces of the stacks. In our periodic TiO_2/TiO/Ti multilayers, the point defects are mainly oxygen vacancies and titanium interstitials in the metallic sub-layer λ_{met}. A change of the calculated TCR from -7.58×10^{-4} to -3.12×10^{-4} K^{-1} is even measured for the lowest periods Λ although the electrical properties show a metallic-like resistivity. Such negative TCRs correlate with the decrease of the grain size (tending and becoming shorter than the electron mean free path) previously observed from XRD and HRTEM. There variations of resistivity vs. period thickness Λ can not be solely explained taking

into account resistivity values of pure Ti and fcc TiO compounds (ρ_{300K}(Ti) = 3.9×10^{-7} Ωm and ρ_{300K}(TiO) = 2.6×10^{-6} Ωm [34]). Our resistivity measurements showed that ρ_{300K} changes from 1.2×10^{-5} down to 5.9×10^{-7} Ωm as the period thickness Λ rises from 14.0 to 54.0 nm, i.e. order of magnitude higher than fcc TiO compound for the shortest period Λ. Thus, the sub-layer dimensions as well as the chemical composition have to be taken into account.

In order to better understand the electrical properties of these multilayers as the period thickness Λ changes, we first analyzed the correlation between the resistivity and the χ parameter. This latter is defined as the metal (λ_{met}) to oxide (λ_{ox}) thickness ratio in a period Λ from:

$$\chi = \frac{\lambda_{met}}{\lambda_{ox}} \qquad (3)$$

In table 1, all parameters (especially the composition) are directly linked to the resistivity and their corresponding TCR values. For most of the samples, the resistivity tends to decrease as a function of the metallic sub-layer thickness λ_{met}. Assuming a simple mixture rule [35], such a decrease can be assigned to the thickness of the metallic sub-layer in the multilayer period Λ, i.e. to the χ parameter. However, the evolution of resistivity at a given temperature (e.g. ρ_{475K} at 475 K as reported in table 1) versus χ parameter does not exhibit a smooth trend. Multilayers with χ = 0.75, 0.69 and 0.89 (Λ = 14.0, 40.5 and 42.5 nm, respectively) strongly deviate from a hypothetic simple exponential relationship between resistivity ρ_{475K} and the metal to oxide thickness ratio χ. Such discrepancy can not be due to some variations of the total thickness of the film t_{tot} since all samples are in-between 335 to 435 nm. Therefore, another and more significant parameter than χ is required to link structure, composition and resistivity. Taking into account EDX analyses samples, which deviates from the hypothetic

exponential relationship between ρ and χ stated before, titanium concentration $C_{\lambda met}$ in the metallic sub-layer versus period Λ also exhibits a more or less randomized evolution. The idea is then to combine the χ and $C_{\lambda met}$ parameters so as to get the real part of titanium in the metallic sub-layer. For the oxide sub-layer, such correction is not relevant since the chemical composition of this sub-layer is always very close to the TiO_2 compound for any oxide sub-layer thickness λ_{ox}. Then, the χ' parameter can be defined as:

$$\chi' = \frac{C_{\lambda met} \times \lambda_{met}}{\lambda_{ox}} \quad (4)$$

It was calculated for all samples (Table 1). A regular and monotonous decrease of the electrical resistivity ρ versus χ' parameter is then obtained. As a result, period Λ, sub-layers thickness λ_{met} and λ_{ox} as well as titanium concentration $C_{\lambda met}$ in the metallic sub-layer can be reliably connected to the resistivity. However, the total thickness t_{tot} of the sample also plays an important role. Indeed, figure 6 shows a direct relationship, where ρ is a function of χ' and t_{tot}. For a fixed temperature, resistivity can be expressed as:

$$\rho = \gamma \exp\left(\frac{\beta t_{total}}{\chi'}\right) \quad (5)$$

where γ and β are constants. It is worth noting that γ has the dimensions of an electrical resistivity. Without any multilayer, one can assume that the χ' parameter approaches infinity and the film can be considered as pure titanium. Then, the resistivity of the film becomes that of the bulk titanium and it can be stated that γ represents the resistivity ρ_0 of pure Ti. From the results presented in figure 6, calculations lead to $\gamma = 5.44\times10^{-7}$ Ω m, which is very close to the resistivity value measured at room temperature for the Ti pure sample (5.80×10^{-7} Ω m). Similarly, $\beta = 2.97\times10^{-7}$ m^{-1} has the dimensions of a reciprocal length. In a manner analogous to the propagation of electromagnetic waves through

391 matter, its physical meaning can be similar to a virtual linear attenuation coefficient
392 intrinsic to the metal oxide interfaces created by the periodic stacks. We suggest that the
393 β parameter characterizes how easily the charge carriers can penetrate through the
394 interfaces of the multilayered structure.
395 Goldfarb et al. [36] correlated the rising resistivity in binary transition metal oxide with
396 the increasing oxygen concentration in the films. By increasing the oxygen content, they
397 claim that oxidation causes depletion of the metal d-band charge carriers in favour of the
398 O 2p valence and so, the carrier concentration decreases. A metal-insulator transition
399 occurs leading to a TCR sign change and an increase of resistivity. In our case, this
400 model can not be taken into account since the oxygen concentration is not the only
401 parameter which influences the electrical properties of TiO_2/TiO/Ti multilayers (Table
402 1). As a result, the resistivity decrease as a function of the χ' parameter has to be
403 discussed taking into account mobility and charge carriers concentration.
404 Hall effect measurements systematically reveal n-type charge carriers for all multilayers.
405 Hall mobility μ versus carrier concentration n is then plotted (Fig. 7). For all samples,
406 log μ decrease as a function of log n. At first, one can notice that mobility as well as
407 carrier concentration are both influenced by the χ' parameter. As χ' rises from 0.523 up
408 to 1.623, the carrier concentration changes from $n = 10^{22}$ to 6×10^{22} cm^{-3} and the Hall
409 mobility varies from μ = 5 to 60 $cm^2V^{-1}s^{-1}$. This evolution agrees with the metallic-like
410 behaviour, which is promoted (resistivity tends to that of Ti bulk and positive sign of the
411 TCR) as χ' increases (Fig. 5). For bulk metals, electron mobility μ is in-between 10^2 to
412 10^3 $cm^2.V^{-1}.s^{-1}$ at 300 K and above room temperature, the temperature dependence
413 follows $\mu \propto T^{-1}$ [37]. For metallic thin films, electron mobility is lower than those
414 measured for bulks due to electron scattering at the grain boundaries [38], with a film's
415 thickness dependence, which is related to the nature of the metal. According to Khojier

and Savaloni [39], the mobility vs. thickness of pure titanium films exhibits a low decrease from $\mu = 1.04\times10^3$ down to 1.00×10^3 $cm^2.V^{-1}.s^{-1}$ as the thickness rises from 12 up to 40 nm. From the same authors, the effect of the temperature has also been investigated (from room temperature until 573 K). A decrease of the mobility (10 to 20% of drop) has been observed with the temperature rising. As a result, period thickness and temperature variations are in the same order of magnitude in our study. However, the pure titanium properties can not be taken as the key parameter, which contributes to the electronic transport properties, even for the thickest period Λ = 50.0 nm, because Hall mobility of the periodic TiO_2/TiO/Ti multilayers is in-between 5 to 60 $cm^2.V^{-1}.s^{-1}$ (more than one order of magnitude lower than pure titanium).

It is worth noting that the mobility is even more influenced by the χ' parameter changes since Hall mobility exhibits values in-between μ = 5 to 60 $cm^2V^{-1}s^{-1}$ as χ' rises from 0.523 up to 1.623, respectively. Considering the order of magnitude of the carrier concentration and its evolution as a function of the carrier mobility, the electrical properties are mainly related to ionized impurity scattering [40]. The theoretical relationship suggested by Seto [41] for mobility dominated by grain boundary scattering is negligible. The observed trend can be rather understood by the Brooks-Herring (BH) theory [42]. In our study, the deposition of TiO_2/TiO/Ti periodic alternations generates several types of defects, which can be point defects, grain boundary discontinuities, interfacial defects (dislocations, stacking faults) and interfaces due to the multilayered structure. The point defects are mainly oxygen vacancies and titanium interstitials (self-interstitial atoms). As a simplifying assumption, it can be firstly assumed that such point defects act as impurities in the scattering phenomena of the charge carriers. Taking into account the screening of the ionized impurities, the BH theoretical relationship links carrier mobility μ_{BH} ($cm^2V^{-1}s^{-1}$) and carrier concentration n (cm^{-3}) according to the

following equation:

$$\mu_{BH} = \frac{C_1}{N_{II}} T^{3/2} \left[\ln\left(C_2 \frac{T^2}{n} \right) \right]^{-1} \quad (6)$$

with C_1 and C_2 are constants given by:

$$C_1 = \frac{128\sqrt{2\pi}\,\varepsilon^2 k_B^{3/2}}{\sqrt{m_{eff}}\,Z^2 e^3} \quad (7)$$

and

$$C_2 = \frac{24 m_{eff}\,\varepsilon k_B^2}{e^2 \hbar^2} \quad (8)$$

where T is the temperature (K), k_B the Boltzmann constant (1.38×10^{-23} JK^{-1}), Z the charge of the scattering centre, ε the permittivity of the material (fixed at 6.25), m_{eff} the effective mass of electron (2.28×10^{-31} kg), e the elementary charge (1.6×10^{-19} As), $\hbar$ the reduced Planck's constant (1.055×10^{-34} Js) and N_{II} the ionized impurity concentration (cm^{-3}). For this study, we have $C_1 = 1.0\times10^{19}$ $m^{-1}V^{-1}s^{-1}K^{-3/2}$ and $C_2 = 1.5\times10^{20}$ $m^{-3}K^{-2}$. Calculations of μ_{BH} vs. n have been performed for the temperature range 300 – 500 K. The carrier concentration has been incrementally increased for the studied range $n = 10^{20}$ - 10^{24} cm^{-3}. Increment I has been defined as a function of the carrier concentration range. Hundred increments have been used for each carrier concentration decade (e.g. $I = 10^{P-2}$ increments with $P = 21$ for $10^{20} < n < 10^{21}$ cm^{-3}). The ionized impurity concentration N_{II} was adjusted in order to fit with experimental data as shown in figure 7. It can be seen that N_{II} increases from $7.30\times10^{-3}\times n$ to $4.35\times10^{-2}\times n$ cm^{-3} when the χ' parameter reduces from 1.623 down to 0.523, respectively. Therefore, the decrease of μ versus n is assumed to be due to an increase of the defects concentration, which act as dominant scattering centres because of the fcc TiO phase occurrence in the metallic sub-layers [43]. This also means that the TiO_2/TiO/Ti periodic multilayers are characterized (supported by

463 HRTEM observations) by a high stacking fault density in the range of 10^{20} cm^{-3}.
464 According to McLachlan [44], these stacking faults can mainly be generated by the
465 formation of titanium and oxygen vacancies since both types of defects can coexist over
466 a large chemical composition in the fcc-TiO_x phase ($0.8<x<1.3$). In addition, since
467 oxygen vacancies exhibit a charge of $Z = 2$, its scattering power is higher than that of
468 single ionized doping elements leading to a reduced mobility and an enhanced carrier
469 concentration.
470
471 **4. Conclusion**
472 TiO_2/TiO/Ti periodic multilayers were successfully prepared by DC reactive magnetron
473 sputtering. The reactive gas pulsing process was used to reach regular periodic
474 alternations with periods Λ in-between 14.0 and 50.0 nm. The oxide sub-layers are
475 composed of rutile and amorphous TiO_2 phases, whereas the metallic sub-layers are
476 formed by a mixture of hcp-titanium and fcc-TiO phases. The difference of metallic and
477 oxide sub-layers crystallinity was evidenced from TEM and HRTEM observations. It
478 was shown that the TiO_2/TiO/Ti periodic structure is partially nanocrystalline with
479 metallic sub-layers, which are better crystallized than the oxide ones. In the metallic sub-
480 layers, the thickness of the fcc-TiO phase was always 4 nm and the remaining
481 corresponded to hcp-Ti. A columnar structure was also pointed out with the occurrence
482 of numerous defects in the crystalline parts. HRTEM investigations confirmed that the
483 columnar growth is maintained in spite of the reactive gas pulses. The chemical
484 composition analyses revealed a homogenous TiO_2 stoichiometric compound in the
485 oxide sub-layers while the titanium concentration strongly varied in the metallic sub-
486 layers. The latter must to be taken into account to understand the electronic transport
487 properties. To this aim, a χ' parameter was defined from the titanium concentration in

488 the metallic sub-layer as well as the metal (λ_{met}) to oxide (λ_{ox}) thickness ratio in a single
489 period Λ. Such χ' parameter was connected to the DC electrical resistivity using an
490 exponential law. TiO_2/TiO/Ti periodic multilayers exhibited a metallic-like behaviour
491 with a TCR sign change and a decrease of resistivity versus χ'. It was mainly assigned to
492 a reduced carrier mobility and an enhanced carrier concentration produced by ionized
493 impurity scattering. The latter was especially favoured by an increase of the defects
494 concentration in the metallic sub-layers. Moreover, the resistivity measurements of these
495 TiO_2/TiO/Ti thin multilayers pointed out some tuneable electrical characteristics versus
496 temperature for an optimized χ' parameter. These results enable some attractive
497 applications of such multilayers, especially for sensors and devices, which often require
498 invariant conduction properties versus temperature.
499
500 **Acknowledgements**
501 This work was supported by the Region Bourgogne (PARI 2011): projet ONOV.

References

[1] Bange K, Ottermann CR, Anderson O, Jeschkowski U, Laube U, Feile R. Thin Solid Films 1991; 197:279.

[2] Watanabe T, Nakajima A, Wang R, Minabe M, Koizumi S, Fujishima A, Hashimoto K. Thin Solid Films 1999;351:260.

[3] Mohammadi MR, Fray DJ. Acta Mater. 2007; 55(13):4455.

[4] Glassford KM, Chelikowsky JR. Phys. Rev. B 1992;46(3):1284.

[5] Radecka M, Rekas M, Czternastek H, Zakrzewska Z, Debrus S. Folia Phys. 1994;26:57.

[6] Alexandrov P, Koprinarova J, Todorov D. Vacuum 1996; 47(11):1333.

[7] Monoy A, Brevet A, Imhoff L, Domenichini B, Lesniewska B, Peterlé PM, Marco de Lucas MC, Bourgeois S. Thin Solid Films 2006;515(2):687.

[8] Brevet A, Marco de Lucas MC, Potin V, Chassagnon R, Imhoff L, Domenichini B, Bourgeois S. J. Phys. D: Appl. Phys. 2009;42:175302.

[9] Regragui M, Jousseaume V, Addou M, Outzourhit A, Bernede JC, El Idrissi B. Thin Solid Films 2001;397:238.

[10] Manno D, Serra A, Di Giulio M, Micocci G, Tepore A. Thin Solid Films 1998;324:44.

[11] Fujii T, Sakata N, Takada J, Miura Y, Daitoh Y, Takano M. J. Mater. Res. 1994;9:1468.

[12] Takikawa H, Matsui T, Sakakibara T, Bendavid A, Martin PJ. Thin Solid Films 1999; 348:145.

[13] Zhang F, Liu X. Thin Solid Films 1998;326:171.

[14] Leinen D, Fernandez A, Espinos JP, Caballero A, Justo A, Gonzalez-Elipe AR. Thin Solid Films 1994;241:175.

[15] Lobl P, Huppertz M, Mergel D. Thin Solid Films 1994;251:72.

[16] Elam JW, Sechrist ZA, George SM. Thin Solid Films 2002;414:43.

[17] Pucker G, Bellutti P, Spinella C, Gatterer K, Cazzanelli M, Pavesi L. J. Appl. Phys. 2000;88(10):6044.

[18] Switzer JA, Hung CJ, Huang LY, Miller FS, Zhou Y, Raub ER, Shumsky MG, Bohannan EW. J. Mater. Res. 1998; 13(4):909.

530 [19] Hmiel AF. J. Vac. Sci. Technol. 1985; A3:592.

531 [20] Serikawa T, Okamoto A. Thin Solid Films 1983; 101:13.

532 [21] Berg S, Blom HO, Larsson T, Nender C. J. Vac. Sci. Technol. 1987;A5(2):202.

533 [22] Hoffman S. Thin Solid Films 1990; 191:335.

534 [23] Billard A, Frantz C. Surf. Coat. Technol. 1993; 59:41.

535 [24] Kusano E, Kinbara A, Baba S. J. Vac. Sci. Technol. 1992; A10 (4):1483.

536 [25] Berg S, Nyberg T. Thin Solid Films 2005; 476:215.

537 [26] Sproul WD, Rudnik PJ, Gogol CA, Mueller RA. Surf. Coat. Technol. 1989; 39-40:499.

538 [27] Cacucci A, Potin V, Imhoff L, Marco de Lucas MC, Martin N. Thin Solid Films
539 2012;520:4778.

540 [28] Sberveglieri G. Sens. Actuators B 1995; 23(2-3):103.

541 [29] Gagiotti G, Galdikas A, Kaciulis S, Mattogno G, Setkus A. J. Appl. Phys. 1994;76(8):4467.

542 [30] Tang H, Prasad K, Sanjinès R, Lévy F. Sens. Actuators B 1995; 26(1-3):71.

543 [31] Martin N, Besnard A, Sthal F, Vaz F, Nouveau C. Appl. Phys. Lett. 2008; 93(6):064102.

544 [32] Martin N, Lintymer J, Gavoille J, Chappé JM, Sthal F, Takadoum J, Vaz F, Rebouta L. Surf.
545 Coat. Technol. 2007; 201:7720.

546 [33] Reiss G, Vancea J, Hoffman H. Phys. Rev. Lett. 1986; 56(19):2100.

547 [34] Wijn HPJ, SpringerMaterials - The Landolt-Börnstein Database.

548 [35] Kasap S, Capper P. Handbook of Photonic Materials, Springer, New-York, Berlin, 2006:32.

549 [36] Goldfarb I, Miao F, Joshua Yang J, Yi W, Strachan JP, Zhang MX, Pickett MD, Medeiros-
550 Ribeiro G, Stanley Williams R. Appl. Phys. A 2012, 107:1.

551 [37] Bube RH, "Electrons in Solids", Academic Press Inc., London, 1992.

552 [38] Chopra KL, Bahl SK, J. Appl. Phys. 1967; 38: 3607.

553 [39] Khojier K, Savaloni H, Vacuum 2010; 84: 770.

554 [40] Minami T. Thin Solid Films 2008; 516:5822.

555 [41] Seto JWY. J. Appl. Phys. 1975; 46:5247.

556 [42] Look DC. Electrical Characterization of GaAs Materials and Devices, Wiley, New-York,

557 USA, 1989; 77.

558 [43] Banakh O, Schmid PE, Sanjinès R, Lévy F. Surf. Coat. Technol. 2002; 151-152:273.

559 [44] McLachlan DS. Phys. Rev. B 1982; 25(4):2285.

560 **Table captions**

561 **Table 1**

562 Summary of dimensional, compositional and electrical characteristics of TiO_2/TiO/Ti
563 periodic multilayer films. Λ = period of TiO_2/TiO/Ti multilayers. t_{tot} = total thickness of
564 the film. λ_{met} = metallic sub-layer thickness. λ_{ox} = oxide sub-layer thickness. $\chi = \lambda_{met}/\lambda_{ox}$
565 as defined from equation (3). $C_{\lambda met}$ = titanium concentration in the metallic sub-layer. χ'
566 $= \chi \times C_{\lambda met}$ as defined from equation (4). TCR = temperature coefficient of resistance
567 calculated from equation (2). ρ_{473K} = DC electrical resistivity at 473 K.

568 **Table 1**
569

Λ (± 0.1 nm)	t_{tot} (± 5 nm)	λ_{met} (± 0.1 nm)	λ_{ox} (± 0.1 nm)	χ (a.u.)	$C_{\lambda met}$ (± 0.02)	χ' (a.u.)	TCR ($\times 10^{-4}$ K^{-1})	ρ_{475K} ($\times 10^{-6}$ Ωm)
14.0	345	6.0	8.0	0.75	0.45	0.338	-4.97	10.5
16.5	350	6.3	10.3	0.61	0.64	0.390	-4.17	7.25
34.6	405	15.3	19.3	0.79	0.51	0.404	-3.12	6.50
18.0	350	7.5	10.5	0.71	0.65	0.464	-7.58	5.10
40.5	325	16.5	24.0	0.69	0.76	0.523	2.17	3.40
45.0	355	24.0	21.0	1.14	0.55	0.629	2.85	2.75
42.5	335	20.0	22.5	0.89	0.75	0.667	4.76	2.53
31.0	410	17.0	14.0	1.21	0.75	0.911	3.42	2.17
40.0	435	22.5	17.5	1.29	0.80	1.029	4.55	2.02
47.3	375	29.5	17.8	1.66	0.70	1.163	10.3	1.55
50.0	405	35	15.0	2.33	0.70	1.633	12.0	1.45

570 **Figure captions**

571 **Figure 1**

572 XRD patterns of $TiO_2/TiO_x/Ti$ multilayered films deposited on (100) silicon wafer for various
573 Λ periodic alternations. The χ' parameter calculated from equation (4) is also indicated. ★ =
574 Si substrate; ● = fcc-TiO; □ hcp-Ti.

575

576 **Figure 2**

577 TEM cross-section observations of $TiO_2/TiO/Ti$ multilayered films deposited on (100) silicon
578 wafer. a) Low magnification BF and b) DF images of the sample period Λ = 14.0 nm. The
579 thickness of metallic and oxide sub-layers is λ_{met} = 6.0 nm and λ_{ox} = 8.0 nm, respectively. The
580 total thickness is t_{tot} = 345 nm. c) Low magnification BF and d) DF images of the sample
581 period Λ = 50.0 nm with λ_{met} = 35.0 nm, λ_{ox} = 15.0 nm and t_{tot} = 405 nm.

582

583 **Figure 3**

584 a) BF micrograph of a multilayer with 8 periods of Λ = 50.0 nm and a total thickness t_{tot} = 405
585 nm. b) A magnified part of this multilayer where metallic and oxide sub-layer thicknesses are
586 λ_{met} = 35.0 nm and λ_{ox} = 15.0 nm, respectively. Poorly crystallized (A and B) and crystallized
587 domains (C, D and E) are shown.

588

589 **Figure 4**

590 (a) The selected area electron diffraction pattern reveals the epitaxial growth of $TiO_2/TiO/Ti$
591 multilayer, by indication of the three phases.

(b) HRTEM micrograph shows a part of the crystallized domains E of Fig. 3b, with an hcp-Ti structure and a zone axis ZA = [0001] (c) HRTEM micrograph shows a crystalline area of the part D in Fig.3b with an fcc-TiO structure and a zone axis [01-1].

(d) HRTEM micrograph shows a rutile phase structure with the d-spacing of the (110) and (200) planes, zone axis ZA = [00-1]. A white arrow indicates the growth direction.

Figure 5

DC electrical resistivity ρ versus temperature T measured on TiO_2/TiO/Ti multilayers for period thickness Λ ranging from 14.0 to 50.0 nm. The χ' parameter defined from equation (4) is systematically indicated.

Figure 6

Linear evolution of the DC electrical resistivity ρ_{300K} at 300 K versus total thickness t_{tot}/χ' parameter ratio. The ρ_{300K}-intercept gives the resistivity of bulk titanium and the slope is related to the capacity of charges carrier to cross through the interfaces of the multilayered structure.

Figure 7

Measured Hall mobility μ as a function of the carrier concentration n of . TiO_2/TiO/Ti multilayers for various χ' parameters defined from equation (4). The solid lines represent the μ versus n evolution calculated from the Brooks-Herring theory assuming that the mobility is dominated by the ionized impurity scattering. The ionized impurity concentration N_{II} is adjusted from the carrier concentration.

615 **Figure 1**

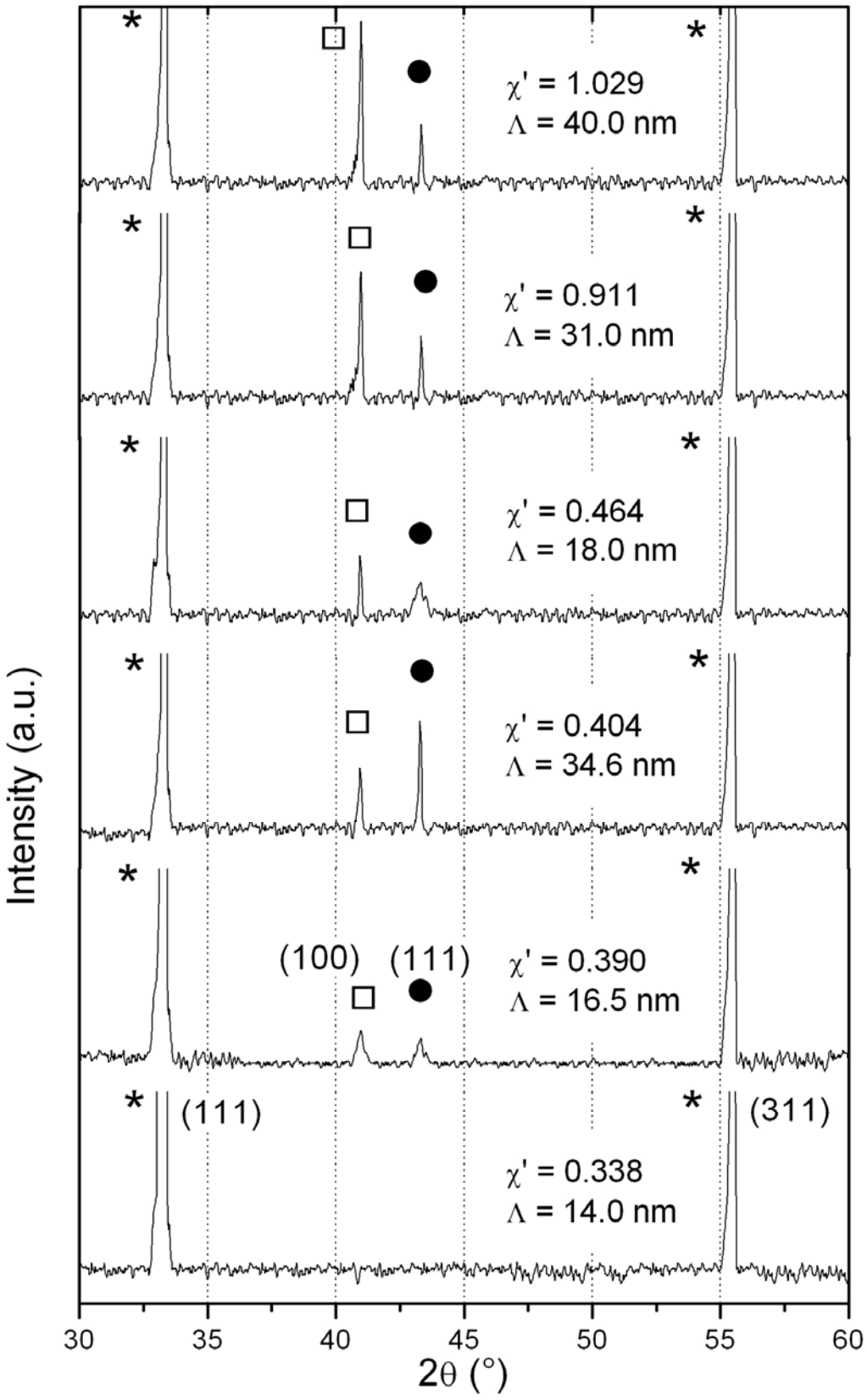

616

617 **Figure 2**

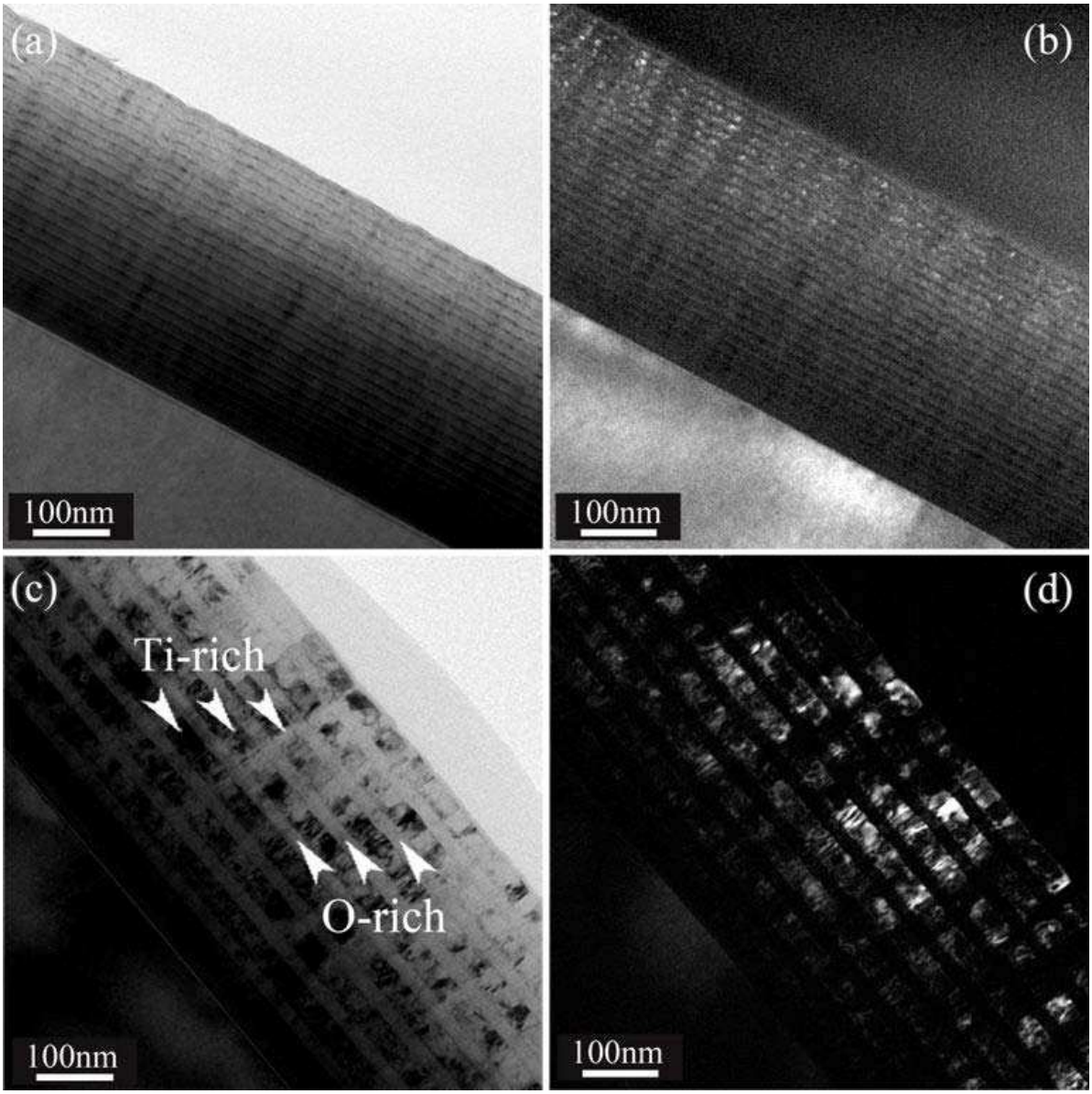

618

619 **Figure 3**

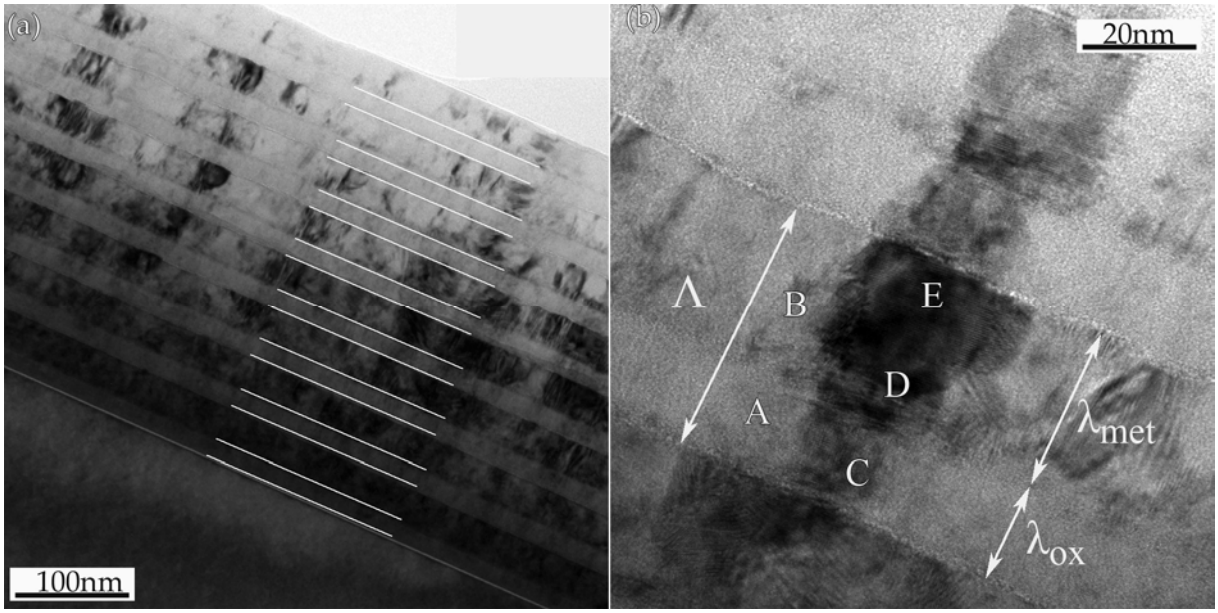

620

621 **Figure 4**

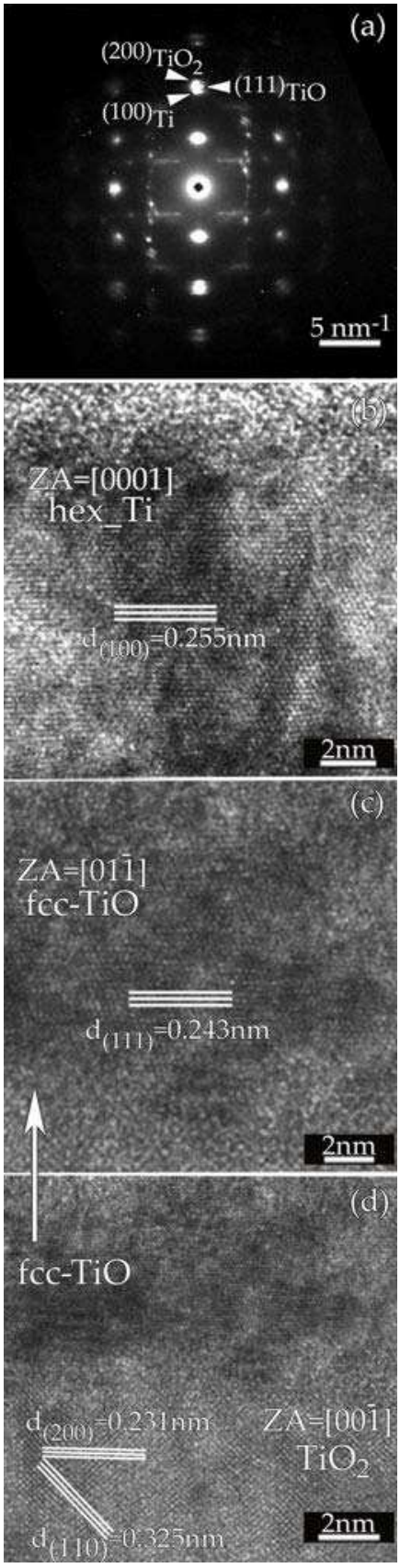

622

623 **Figure 5**

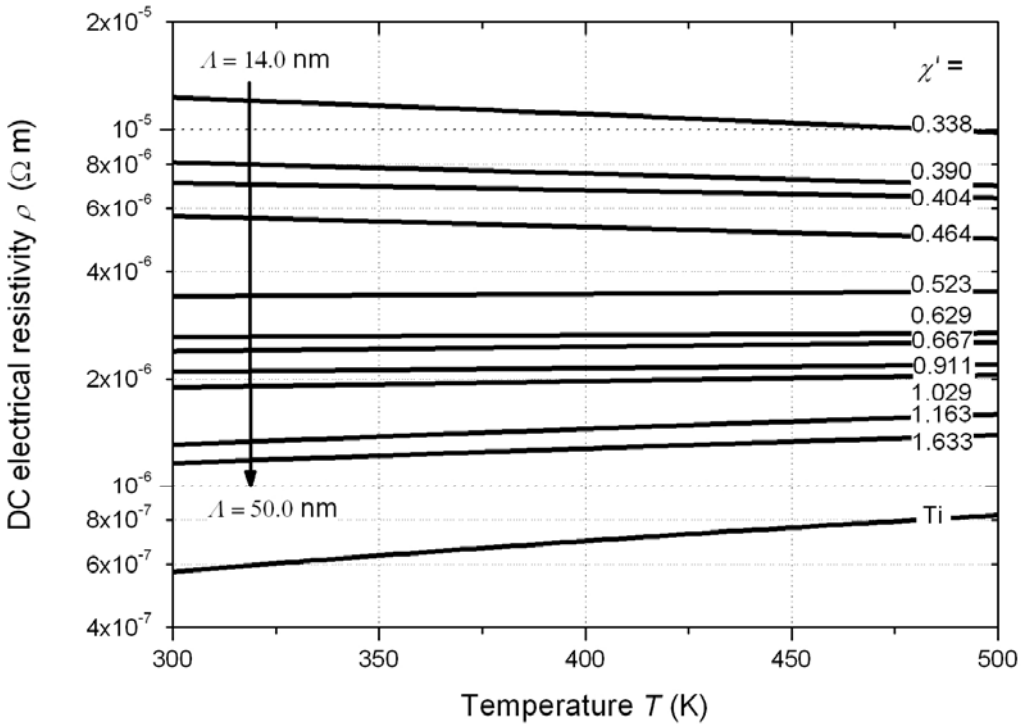

624

625 **Figure 6**

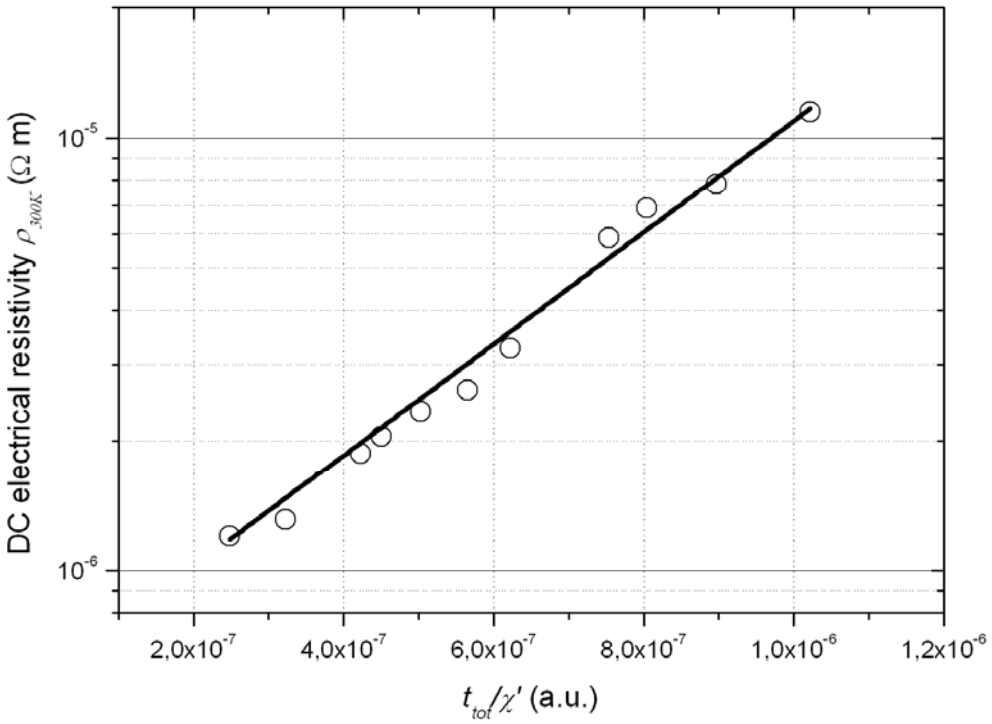

626

627 **Figure 7**

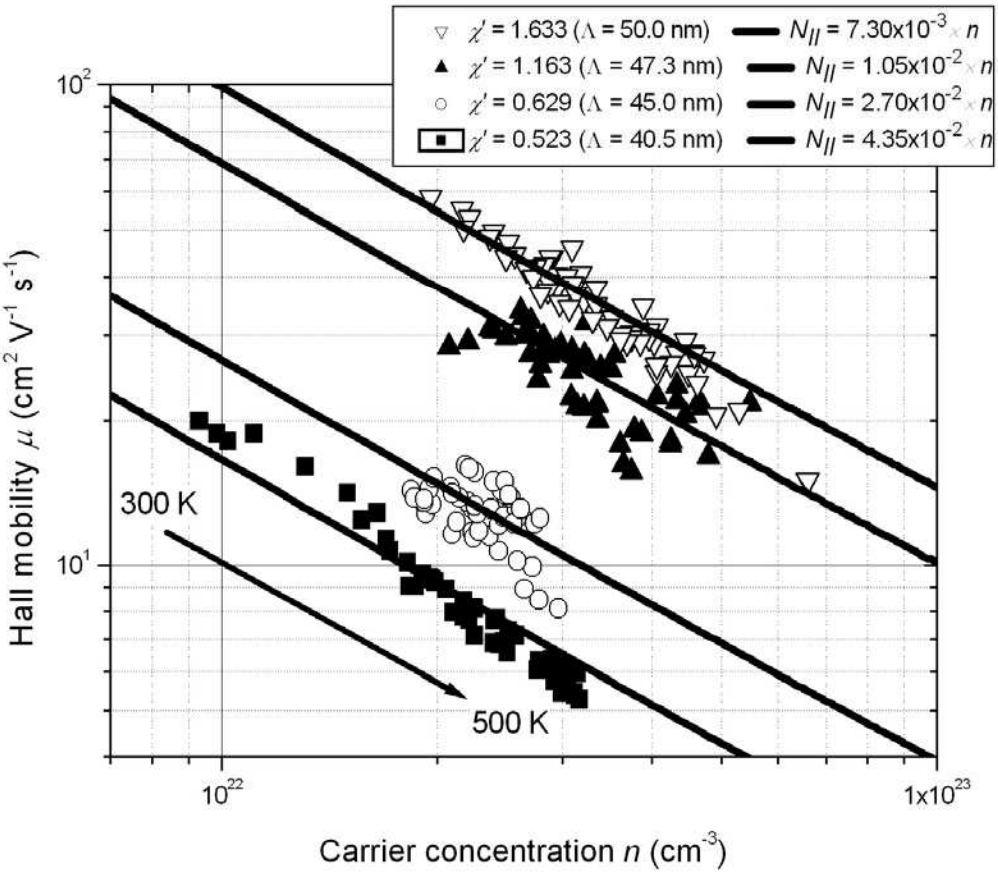

628